Proper Orthogonal Decomposition and Spectral Analysis of a Wall-Mounted Square Cylinder Wake

Henrique Fanini Leite[1], Ana Cristina Avelar[2], Leandra de Abreu[1], Daniel Schuch[3], André Cavalieri[1]

Leite HF (ID) https://orcid.org/0000-0002-7303-9411

Avelar AC (ID) https://orcid.org/000-0002-0333-4570

Abreu L (ID) https://orcid.org/0000-0002-3899-6144

Schuch D (ID) https://orcid.org/0000-0001-5977-4519

Cavalieri A (ID) https://orcid.org/0000-0003-4283-0232

ABSTRACT: The flow patterns over a finite square cylinder of aspect ratio of 3 were analyzed experimentally in a subsonic wind tunnel using the time-resolved particle image velocimetry (TR - PIV) techniques. The near wake flow structures and vortex shedding characteristics were investigated using mean flow analysis, spectral analysis and proper orthogonal decomposition (POD). The cylinders were fixed on a elliptical leading edge flat plate, creating a boundary layer which interacted with the cylinder wake. The 2D PIV measurements were conducted at a low horizontal plane, $z/h = 0.3$, to investigate possible boundary layer interactions. Due to the complexity of the phenomena, the flow was characterized both in terms of average behavior and time-resolved velocity fields. Both symmetrical and anti-symmetrical vortices structures occur in the cylinder wake, which can be identified based on the coefficients of the first four POD modes. The results indicated that the alternating Karman vortex structures are dominant, described by the first two POD modes.

KEYWORDS: PIV method application, Proper orthogonal decomposition, Finite cylinders, Unsteady flow, Time-resolved PIV.

INTRODUCTION

The flow around a cylinder has been a subject of investigation since the beginning of fluid mechanics as a science. Starting from D'Alembert's paradox, this type of flow eluded scientists due to its simple geometry and complex flow structure, which presents many patterns, depending on Reynolds number, ranging from quasi-potential flow for very low Reynolds, to complex vortex-shedding mechanisms at higher Reynolds values. Besides its academic importance, the unsteady characteristics of cylinder wakes make this an excellent phenomenon to validate unsteady computational fluid dynamics (CFD) models. Evidently, turbulence associated instabilities will be more pronounced in the real-life wake, but parameters such as vortex shedding frequency and shedding type, as well as mean velocity fields, must match. Another possible application is in preventing flutter onset in all sorts of structures. Due to its simple format, a cylinder can be used as a model for structures ranging from a skyscraper to an antenna. In aerospace applications, antenna flutter is hardly a problem for the vehicle structural integrity, but it may damage the antenna

1. Departamento de Ciência e Tecnologia Aeroespacial – Instituto Tecnológico de Aeronáutica – Divisão de Aeronáutica – São José dos Campos/SP – Brazil
2. Departamento de Ciência e Tecnologia Aeroespacial – Instituto de Aeronáutica e Espaço – Divisão de Aerodinâmica – São José dos Campos/SP – Brazil
3. Departamento de Ciência e Tecnologia Aeroespacial – Instituto de Aeronáutica e Espaço – Divisão de Ciências Atmosféricas – São José dos Campos/SP – Brazil

itself, which may cause failure in telemetry. By determining the fundamental frequencies associated with vortex shedding, it is possible to predict possible structural interactions induced by it. Moreover, the cylinder wake can serve as a model for understanding general blunt bodies' wakes and, thus, the first step in developing ways to reduce wake induced drag in a huge variety of applications.

The wake behind 2D cylinders has been extensively investigated, both experimentally and through numerical simulations, and while some questions remain, most of their aspects are well understood, at least at the empirical level (Williamson 1996). However, in most practical applications, cylinder structures have one free end and the other end attached to a surface, often with aspect ratios (H/d, defined as the ratio between height and diameter) lower than 10, and therefore cannot be considered 2D. For these types of cylinders, there may be different vortex shedding mechanisms, depending on geometry, which interact in complex ways. Pioneering studies have shown that the type of wake depends strongly on the cylinder's aspect ratio. Quasi-periodical, Karmann-like vortex shedding predominates up to a critical value $(H/d)cr$, below which it is suppressed by the tip-induced downwash (Kawamura *et al.* 1984; Sakamoto and Arie, 1983; Pattenden *et al.* 2005). While some authors describe the existence of an arch-type symmetrical vortex shedding pattern (Sakamoto and Arie 1983; Wang and Zhou 2009), which is favored by lower aspect ratios and the upwash and downwash induced by the base and tip streamwise vortices, others only identified the anti-symmetric pattern (Bourgeois *et al.* 2011; Hosseni *et al.* 2012). For circular cross-section cylinders, values for $(H/d)cr$ range from 2.5 to 6, depending on the boundary layer thickness. For a square cross-section, it has been suggested that $(H/d)cr \sim 2$ (Sakamoto and Arie 1983; Okamoto and Yagita 1973). Moreover, both symmetrical and anti-symmetrical types of shedding were observed in well above and below critical aspect ratios, with spanwise variations in type predominance within the same cylinder (Wang and Zhou 2009; Wang 2012). For cylinders with a square cross-section, one would expect a stronger spanwise vortex shedding, as flow detachment is stronger and more abrupt than in the circular cross-section case (Wang and Zhou 2009; Leite *et al.* 2016; Wang 2012).

In terms of streamwise vortices, two main structures can be identified. Two streamwise vortices form at the free end, the so-called tip vortices, which arise from the coupling of the tip-induced downwash and the upwash along the side wall (Kawamura *et al.* 1984; Wang and Zhou 2009; Etzold and Fiedler, 1976). In addition to the tip vortices, a second pair of streamwise vortices was detected originating the tip surface, where oil visualization indicated a swirling pattern (Roh and Park 2003). Pattenden *et al.* (2005), however, found no evidence of this second pair in cylinders of $(H/d) = 1$. In cylinders with (H/d) above a certain value, which depends strongly on boundary layer thickness, there is another pair of streamwise base vortices originating at the junction between the cylinder and the wall (Hosseni *et al.* 2012; Tanaka and Murata, 1999; Wang *et al.* 2006). Bourgeois *et al.* (2011) provided a different hypothesis, according to which the streamwise vorticity is the result of upstream bending of the spanwise vortex structure. Wang *et al.* (2006) investigated three boundary layer thickness in a $(H/d) = 5$ square cylinder and showed that the probability of anti-symmetrical vortex shedding at $(z/d) = 1$ was reduced from 84% to 34.5% with an increase in boundary layer thickness from 0.07d to 0.245d. At $(z/d) = 4$, the trend was opposite, with the probability of anti-symmetrical shedding going from 19.5% to 46.5%. These results indicate a strong association between induced upwash or downwash and spanwise vortex shedding.

Wang and Zhou (2009) have measured the shedding frequencies throughout a $(H/d) = 7$ cylinder span and found that the peak occurs at the same frequency in all locations, even 10 diameters downstream. The authors suggested that this result implied that the tip and base vortices may separate from the cylinder at the same frequency as spanwise vortices, and each of the three types of vortices may be part of the same entity of the organized structure. For $(H/d) > 7$, however, the spanwise shedding frequency may vary in a cellular fashion (Adaramola *et al.* 2006; Sakamoto and Oiwake 1984; Uematsu *et al.* 1990). Park and Lee (2002) have found a secondary frequency peak associated with the counter rotating vortices formed at the free end, which is rapidly suppressed downstream.

Although widely studied, the exact mechanisms behind these vortex structures and the interaction patterns between them are still not completely understood. There is no consensus on how the streamwise vortices interact with the spanwise vortex sheet. Based on phase-averaged data in a series of PIV instant velocity fields of the wake of a $(H/d) = 4$ square cylinder, Bourgeois *et al.* (2011) proposed the existence of connector strands, which are formed by the upstream bending

of vertical vortices due to the free end shear layer and that connect to the anteceding structure shed on the opposite side of the wake. Other authors have presented similar results, with dipole wakes forming half-loop structures and quadrupole wakes forming full-loop structures (Hosseni *et al.* 2012). These models do not take into account the symmetrical shedding, since the phase averaging technique did not indicate any dominant symmetrical shedding structure. Wang and Zhou (2009) proposed a model where spanwise vortices from both sides of the cylinder are connected with each other near the free end, forming an arch-type vortex. This arch-type vortex structure has two legs that join each other near to the cylinder free end, that is, they form a full loop structure similar to the one proposed by Hosseni *et al.* (2012). Under the influence of the free-end downwash flow and the boundary layer over the wall, both the upper and the lower parts of the arch-type structure are inclined upstream, accounting for the tip and base vortices. In addition, they postulate the existence of a horseshoe vortex near the base due to observations from other authors. The legs can be either symmetrically arranged or staggered, with no significant distinction between the structures. While the model proposed by Bourgeois *et al.* (2011) ignores symmetrical vortex shedding, the model proposed by Wang and Zhou (2009) does not explain how unified shedding structures can lead to different proportions of symmetrical and anti-symmetrical shedding throughout the cylinder span. Other authors propose models in which streamwise vortices are not connected to the spanwise vortex street (Kawamura *et al.* 1984; Etzold and Fiedler 1976; Wang *et al.* 2005).

Although the 2D nature of our PIV measurements presents a serious limitation, mean and time-resolved vertical and horizontal velocity maps are the most direct way of diagnosing the flow, being able to, if not completely define observed structures, provide significant insight into its behavior. The purpose of this paper is to investigate the combined use of time-resolved PIV data and the POD technique not only to characterize the main organized flow structures but as a guide for instant-velocity map visualization and spectral analysis. Thus, by analyzing the values of the POD modes coefficients, one can identify snapshots where a particular flow structure is prominent. On the other hand, comparing the frequency spectrum at random points within the wake with those taken in vortex cores or saddle points of some of the POD modes, it is possible to identify the overall contribution of that particular mode to the frequency spectrum. In the following sections, these techniques will be explained and their functionality investigated.

METHODOLOGY

The main data source for this investigation were horizontal and vertical 2D velocity fields, measured using time-resolved PIV. Tests were performed for a wide range of cases, but this paper focuses on a single one: the flow at the horizontal plane near the base, at *z/h = 0.3*, for a square cross-section cylinder of *AR = 3*. The cylinder aspect ratio was chosen to enable both symmetric and anti-symmetric vortex shedding patterns, albeit predominance of the latter is expected (Wang and Zhou 2009). Shedding patterns at the measuring plane *z/h = 0.3* were strongly influenced by the boundary layer, while well within the coherent shedding region (Wang *et al.* 2006). Flow speed was 20 m/s, corresponding to a Reynolds number of $Re_d = 54000$, based on the square cross-section side. Following the results of this analysis, a wider study will be performed, with all available combinations of flow speed, geometry and measured plane considered (48 in total).

Tests were carried out in the TA-3 wind tunnel, which is a closed-circuit wind tunnel with an open test section. The maximum speed through its empty test section is around 38 m/s and the turbulence level is 2%. The open test section facilitated both optical and physical access to the model, allowing greater flexibility in experiment configuration. Four different cylinder models were tested, two with circular cross-section, 40 mm diameter and aspect ratios of 3 and 6, and two with square cross-section, 40 mm side and aspect ratios of 3 and 6. In addition, both AR6 cylinders had pressure taps. Figure 1 presents a regular AR6 cylinder under the laser light sheet in the TA-3 test section.

PARTICLE IMAGE VELOCIMETRY

For the PIV measurements, the laser sheet was generated by a Litron pulsed Nd:YLF laser with 10 mJ of energy per cavity, at 1 kHz. The whole flow was seeded with polyethylene glycol smoke using a high-volume liquid seeding generator from
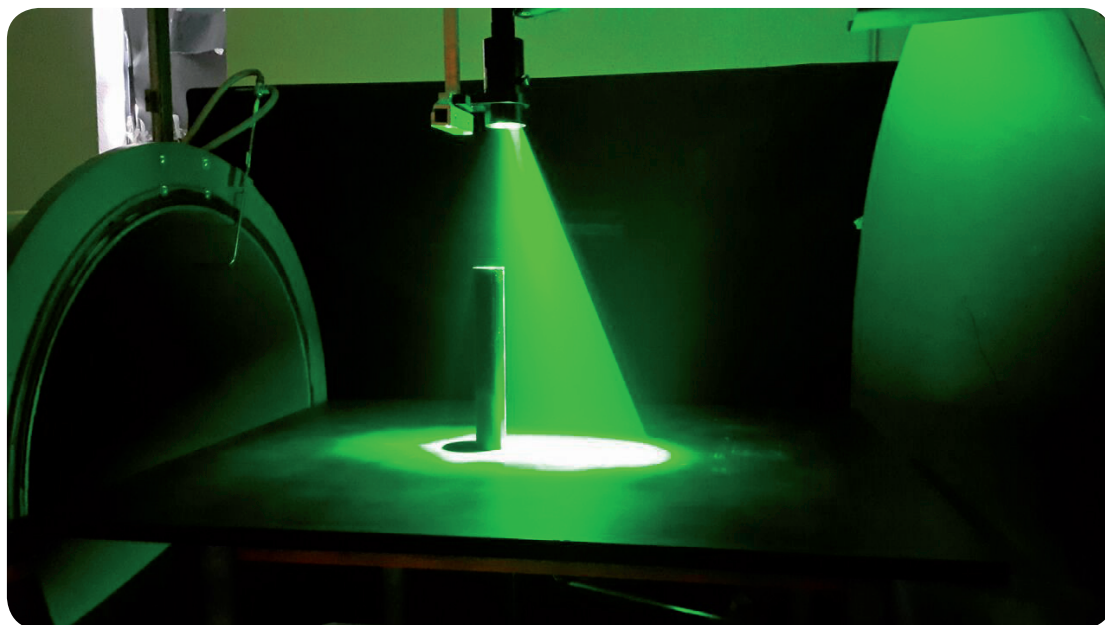
Figure 1. A cylinder model under the PIV laser sheet in the TA-3 wind tunnel.

Nova Instruments. A 105 mm focal lens with f# equal to 5.6 was used on a SpeedSense 9020 CMOS camera, 1 kHz, with full resolution of 1152 × 896 pixels. A light arm from Dantec Dynamics was used to conduct the laser beam, and, consequently, the light sheet to the region of interest. Dynamic Studio software, also from Dantec, was used for data acquisition and processing. To avoid laser reflections, both model and plate were painted in flat black. At measurements near the plate surface, lens aperture was reduced, achieving an f# value of 8.0. A great effort was made to keep the laser sheet uniform at 2 mm thickness.

A total of 663 images were taken for each condition. This was due to internal camera memory limitations. Velocity fields were determined by adaptive correlation, a method with higher computational cost, but which is able to provide better results in regions of strong velocity gradients. This method was chosen due to the presence of intense velocity variations in the detachment region and in the boundaries of the reverse flow region. It iteratively optimizes the size and shape of each interrogation area to better adapt to local flow gradients and seeding densities, thus optimizing correlation conditions at each interrogation window (Wang 2015). Window interrogation size was 32 × 32 pixels and 50% of overlap was considered.

PROPER ORTHOGONAL DECOMPOSITION

The proper orthogonal decomposition (POD) is a quantitative method that has been increasingly applied to instantaneous whole-filed measurement techniques, such as PIV, to identify coherent structures. The POD technique provides a basis for the modal decomposition of a set of data into an ensemble of functions, called POD modes. The first modes concentrate the most energy and represent the largest and most coherent structures of the flow. Therefore, if the flow dynamics present only a few predominant structures, the data can often be represented using just some of the first modes. This method has been successfully used in describing various types of flows, such as mixing layers, jets, channel flows and cylinder wakes. The use of POD method in the PIV data has previously been reported by Graftieaux *et al.* (2001), Meyer *et al.* (2007), Wang (2012) and Pedersen and Meyer (2002).

The snapshot POD method was the selected approach to analyze the experimental data. In this method, each snapshot corresponds to an instantaneous PIV data of the flow field. The present snapshot POD follows the procedure outlined by Meyer *et al.* (2007) and Wang (2012).

The first step is to calculate the mean velocity field and subtract it from each snapshot, so that the analysis is done only for the fluctuation parts of the velocity components (u_i^n, v_i^n), where u and v denote the fluctuation velocity in streamwise and lateral directions, the index n runs through the N snapshots, and i runs through the M positions of velocity vectors in a given snapshot.

All fluctuating velocity components from N snapshots are arranged in a matrix U:

$$U = [u^1, u^2 \ldots u^N] = \begin{bmatrix} u_1^1 & u_1^2 & \ldots & u_1^2 \\ \vdots & \vdots & \ddots & \vdots \\ u_M^1 & u_M^2 & \ldots & u_M^N \\ v_1^1 & v_1^2 & \ldots & v_1^N \\ \vdots & \vdots & \ddots & \vdots \\ v_M^1 & v_M^1 & \ldots & v_M^1 \end{bmatrix}$$

Thus, the autocovariance matrix C is created:

$$C = U^T U$$

A set of N eigenvalues λ^i and corresponding set of eigenvectors A^i, which satisfy:

$$C A^i = \lambda^i A^i$$

The eigenvalues are ordered by decreasing values as $\lambda^1 > \lambda^2 \ldots > \lambda^N > 0$. The normalized POD modes φ^i are constructed from the projection of the eigenvectors A^i:

$$\varphi^i = \frac{\sum_1^N A_n^i u^n}{\left\| \sum_1^N A_n^i u^n \right\|}, \quad i = 1,2, \ldots, N$$

The discrete 2-norm is defined as:

$$\|y\| = \sqrt{y_1^2 + y_2^2 + \cdots + y_M^2}$$

Each snapshot can be expanded in a series of POD modes with expansion coefficients a^i for each φ^i. The coefficients a^i, also called POD coefficients, are determined by projecting the fluctuating part of the velocity field in POD modes:

$$a^n = \Psi^T u^n$$

where $\Psi = [\varphi^1, \varphi^2, \ldots, \varphi^N]$. Then, the expansion of the fluctuation part of a snapshot n is obtained from:

$$u^n = \sum_1^N a_i^n \varphi^i = \Psi a^n$$

The decreasing ordering of the eigenvalues and eigenvectors ensures that the most important modes in terms of energy are the first modes. Although not always the case, this usually means that the first modes will be associated with large-scale flow structures. If a flow has dominant flow structures, these are therefore reflected in the first POD modes and hence a given snapshot can often be reconstructed satisfactorily using only the first few modes. More details on POD can be found in Holmes *et al.* (1998), Meyer *et al.* (2007) and Wang (2012). The snapshot POD was made using MATLAB®.

SPECTRAL ANALYSIS

Calculation of the spectral energy density of the flow components provides a measure of the relative importance of different scales of turbulence. Turbulence spectra information can be used to improve the understanding of transport phenomena in turbulent fluids, the heat flux (as the gases or water vapor) in an interface region, the effect of geometry (or obstacles) into the flow and can improve the parametrization of higher order turbulence closure models.

The turbulence kinetic energy (TKE) is the mean kinetic energy per unit mass associated with eddies in turbulent flow and can be written like:

$$TKE = 0.5\left(\overline{u'^2} + \overline{v'^2} + \overline{w'^2}\right)$$

An important indicator of eddy scale is the position of the peak of the u, v and w spectra. The spectral energy densities $S_u(k)$, $S_v(k)$ and $S_w(k)$, where k represents the wavenumber, are the Fourier transforms of single-point, time-delayed functions and represent the contribution of different eddy scales to TKE. The energy spectra can be classified into three scales: the energy-containing range, where the energy is produced, the inertial subrange where both energy production and energy loss to dissipation are insignificant, but energy is handed down to smaller and smaller scales and finally the dissipation range, where the kinetic energy is dissipated by viscous effect. Figure 2 illustrates the three scales, as well as the proportionality factors for k.
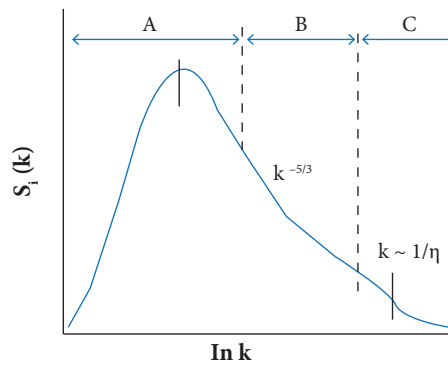
Figure 2. Idealized energy spectrum with three regions: the energy containing range (A), inertial subrange (B) and the dissipation range, $Si(i = u, v, w)$ is the spectral energy density. Adapted from Kaimal and Finnigan (1994).

The main objectives of the spectral analysis were to identify vortex emission frequencies and to determine specific contributions of each POD mode. Fluctuations of the u and v components, as well as the TKE, were analyzed in specific points, which were determined by the results of the POD analysis. These points represented vortex cores or saddle points of the most energetic POD modes, and were selected hoping that they would provide information on this mode. By definition, at a 2D saddle point or vortex core, the velocity is zero. Thus, by selecting a saddle point in the velocity field representation of a certain mode, its contribution to the total velocity fluctuation at this specific point will be null. If the selected mode is responsible for a specific frequency of the spectrum, this particular frequency will not be detected at the spectral analysis of the velocity time series at the selected point, allowing its identification in comparison with the spectrum taken at other points.

RESULTS AND DISCUSSION

Experimental data analysis focused mainly in detecting coherent structures within the flow and dominant vortex-shedding frequencies. Such structures can be identified by many different methods, varying in precision and complexity. For this study, the following techniques were used:

- Spectral analysis of time resolved horizontal and vertical velocity components, as well as turbulent kinetic energy in a range of positions within the cylinders' wake.
- Visualization of instant velocity fields and time-averaged velocity fields.
- Snapshot POD of the entire velocity field.

The time-averaged velocity field, or mean velocity field, is helpful to identify coherent structures in an unsteady flow. Although periodic structures, like vortex shedding, do not appear in these results, mean wake structures can provide information regarding stationary vortex, as well as help identify vortex-shedding mechanisms (Levold, 2012). This sort of analysis, however, can also yield similar results to very different behaviors.

POD ANALYSIS

The processed PIV data will be presented as mean vector fields and POD modes. The data from the cross-section $z/h = 0.30$ is based on 663 snapshots. To investigate the dependence of the number of snapshots, the analysis has been repeated for 200 snapshots. The results were qualitatively the same of those based on 663 snapshots, but some random variations appeared, like slightly asymmetrical flow structures. A convergence analysis was also performed, indicating that the accuracy of POD based on 663 snapshots was satisfactory up to the sixth mode.

The eigenvalues (λ) and its cumulative sum representing the energy of each POD mode are shown in Fig. 3. POD modes 1 and 2 are significantly stronger than the others. They together represent about 53% of the energy in velocity fluctuations, whereas modes 3 and 4 together represent only about 7%.
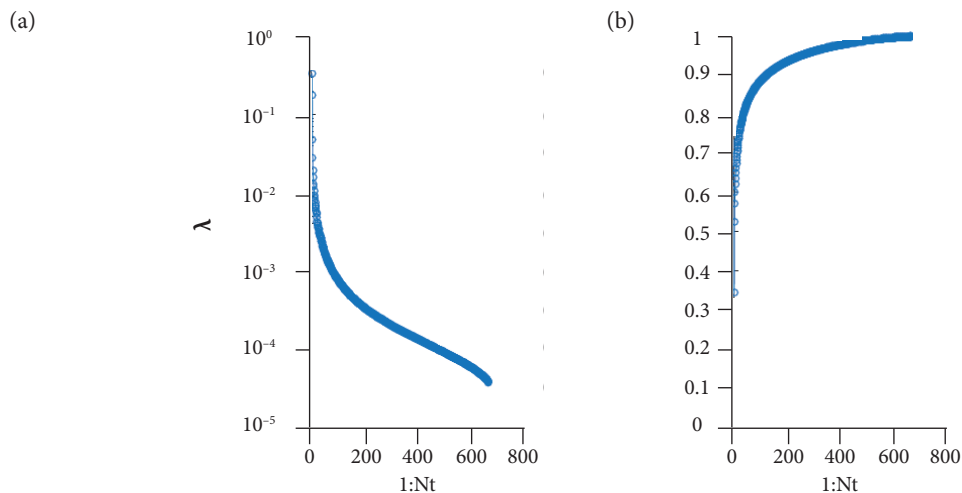
Figure 3. POD eigenvalues (a) and cumulative energy (b) from each POD mode.

Figure 4 shows the first four POD modes of u and v for a 2D square cylinder wake in a position $z/h = 0.3$. One can see that the contour structures of modes 1 and 2 are highly correlated. Particularly, mode 2 can be interpreted as a streamwise shift of mode 1, with the phase difference of about 1/4 of the shedding circle. For modes 1 and 2, the contours with positive and negative values present an alternating pattern, the contours of φ are anti-symmetrical about the wake centerline, which inherently resembles the alternating von Karman vortex structure. The pattern of modes 3 and 4 is different from those of the first two modes, as shown in Fig. 4. The contours of are symmetrical about the wake centerline. This correlates well with previous reports, which indicate a predominance of Karman-type vortex shedding in square cylinders of aspect ratio above $h/L = 2$.

The vortices are convected downstream and the first two POD modes seem to describe two phases of the convective motion. The circular distribution of the a_1 and a_2 coefficients, shown in Fig. 5, suggests a cyclic variation of POD modes 1 and 2, which

is exactly what is expected if two POD modes describe different phases of a vortex formation pattern. The a_1 and a_2 coefficients change similarly to cosine and sine functions, respectively, in a time-resolved study of the flow. The random variations from a simple circle in Fig. 5 accounts for the influence of turbulence in terms of both local velocity fluctuations and irregularities in the creation of the vortices in the wake. Another factor that supports the idea that modes 1 and 2 correspond to a von Karman shedding pattern is the oscillatory nature of its coefficients, as presented in Fig. 6. The alternation between negative and positive
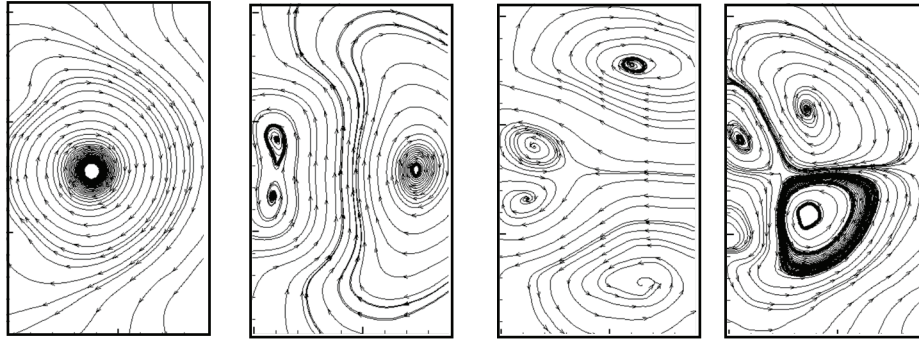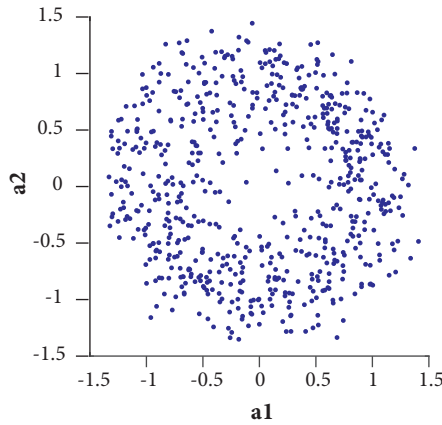

Figure 4. POD modes in the z/h = 0.30 plane.

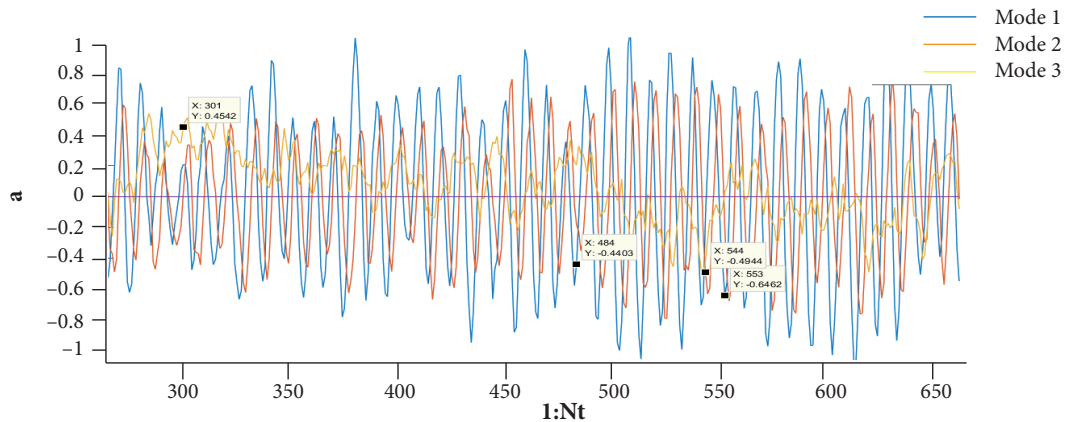**Figure 5.** Distribution of the first and second POD modes.

Figure 6. POD coefficients for a part of the 663 snapshots, with selected snapshots coefficients highlighted.

values corresponds to the emission of clockwise and anti-clockwise vortexes, while the relationship between modes 1 and 2 is related to the interaction between the vortexes. Examples of the vortex shedding pattern associated with POD modes 1 and 2 are shown using snapshots and their reconstructions in Fig. 7. Based on the energy distribution for POD modes, the main features of these wake vortices are well described by the first four modes.
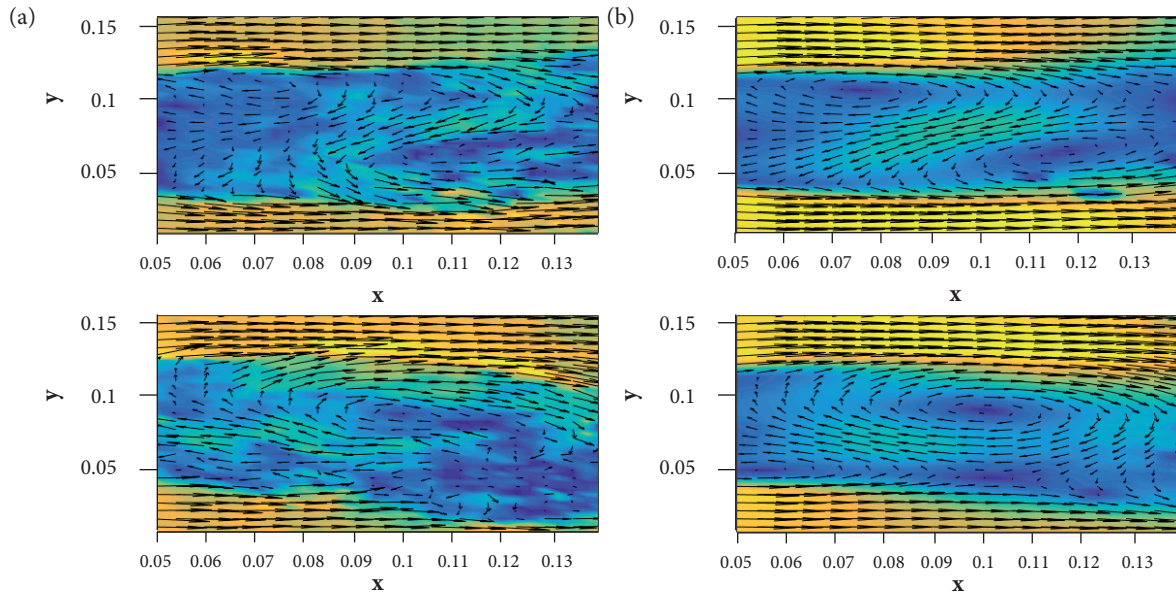
Figure 7. Snapshot (a) and reconstruction (b) using the first four POD modes.

It is interesting to observe how different combinations of just four modes can lead to a great variety of velocity fields. This, in turn, indicates that even small variations in the relative weight of each mode can lead to important changes in flow behavior. This observation is crucial to elucidate the many flow structures detected by instant velocity field visualization.

However, one must bear in mind, however, that the analysis of POD modes energetic contributions takes into account the whole time length of the experiment. As shown in Fig. 6, the instant value of the POD coefficients varies considerably, indicating important time-dependent variations in flow behavior, as will be discussed in the following section.
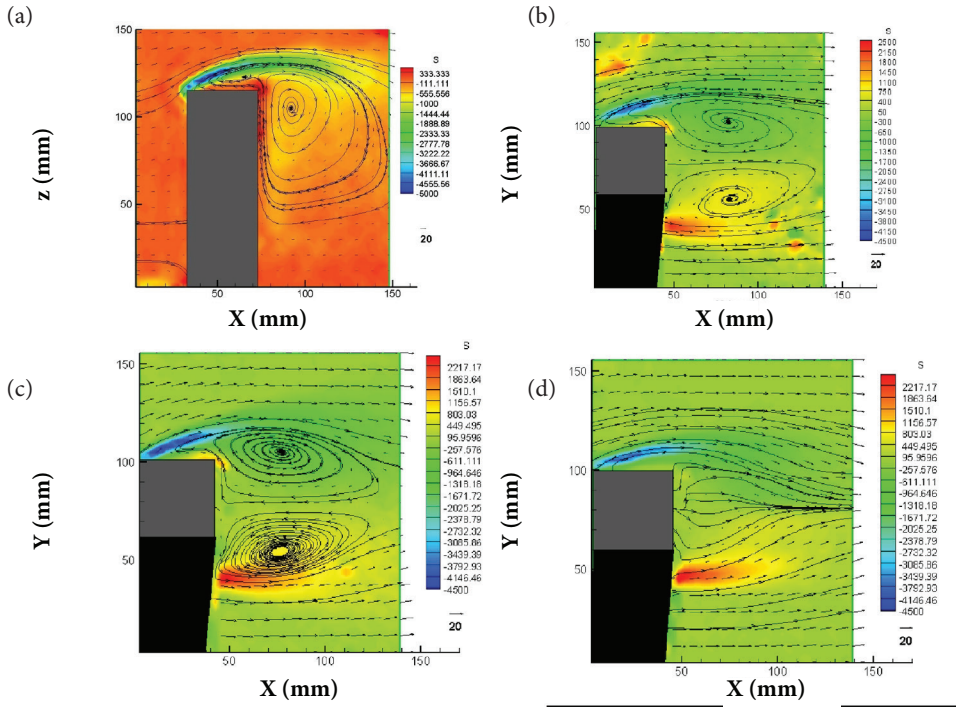
TIME-AVERAGED AND INSTANT VELOCITY FIELDS

Time-averaged velocity fields for the AR3 square cylinder are presented in Fig. 8. Streamlines are only to facilitate interpretation, and do not provide information regarding velocity magnitude. Color maps represent vorticity ("S"), in (1/s). Scales are the same for the horizontal plane images, but different for vertical plane. The gray area represents the cylinder, while the black one represents regions that could not be reached by the laser plane. At the bottom right, the 20 m/s reference vector is represented.

Of the vortexes represented in Fig. 8, only the vertical one, Fig. 8a, is stationary. Another important information is that horizontal vortex core positions do not change considerably from the middle to the bottom plane. This suggests that the influence of the free end-induced downwash is equally felt at both positions, or that the horizontal flow mechanisms predominate over it. At the top plane, no vortex structure can be noticed, which suggests that the main flow and the tip and vertical arch vortexes predominate. In addition, a separation bubble could be detected at the tip, which is induced by the cylinder's sharp edge.

The horseshoe vortex and the tip vortex could not be detected, since they would induce vertical velocity variations at the edges of the cylinder, undetectable by the 2D PIV at horizontal planes, and far from the vertical plane shown in Fig. 8.

Figure 9 presents instant horizontal velocity fields at $z/h = 0.3$. These were taken at cautiously selected moments, correspondent to the peaks in certain values of the POD mode coefficients. Figure 9b corresponds to image number 553, it exhibits a predominance

Figure 8. Time-averaged velocity fields and vorticity maps for: (a) vertical plane; (b) bottom horizontal plane (z/h = 0.3); (c) middle horizontal plane (60 mm, or z/h = 0.5) and (d) tip.
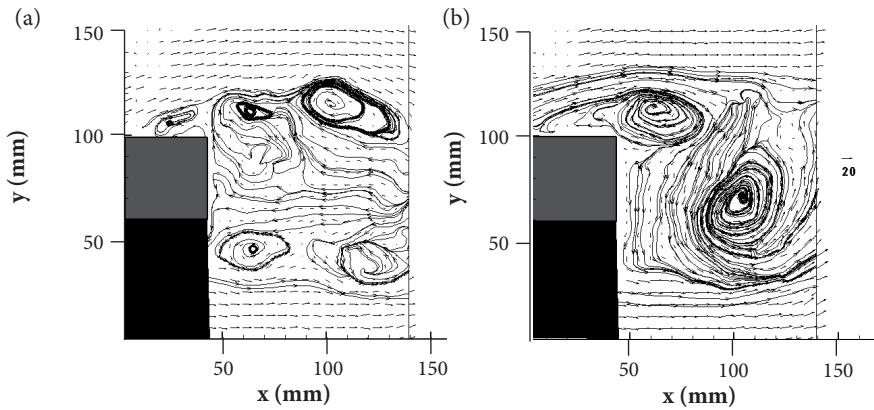
Figure 9. Instant velocity fields for an AR3 square section cylinder, z/h = 0.3. (a) symmetric vortex shedding; (b) anti-symmetric vortex shedding.

of modes 1 and 2, which represent Karman vortex shedding. In it, this structure is clearly predominant. Figure 9a corresponds to image 301, which corresponds to a peak in the value of POD mode 3. Thus, it becomes clear that mode 3 is associated with symmetrical vortex shedding.

The results presented in Fig. 9 indicate that the attempt to determine a critical aspect ratio – dependent on boundary layer thickness and incoming turbulence intensity – after which vortex shedding behavior turns from symmetrical to anti-symmetrical is not an accurate way of describing the flow. Although the symmetric modes were shown to contain less than 7% flow energy, they still play an important part in flow behavior, even predominating over other modes at times. In reality, both symmetrical

and anti-symmetrical mechanisms coexist, each predominating at different moments. It remains unclear what makes each mode predominant, or if this phenomenon is part of a greater pattern. Unfortunately, data was collected during slightly more than one second, making it impossible to investigate if there is a defined frequency for the predominance of each mode.

In addition to the clear vortex shedding patterns, at times complicated patterns emerged, corresponding to images where the three first POD modes coefficients were of comparable magnitude. Figure 10 exemplifies this.

Figure 10a, corresponding to series image 544, was taken at a point where the coefficients of all three modes were negative and had a relatively low magnitude. It is possible to identify a Karman vortex-shedding pattern, but the upstream vortex has two cores, both rotating clockwise (which means there is some sort of saddle point between them, or a very small anti-clockwise rotating region), whereas a third, secondary anti-clockwise vortex structure is present at the bottom, slightly upstream from the two other cores. Downstream, there is a well-defined vortex, which rotates anti-clockwise and forms a pair with the two-cored vortex structure. The low magnitude of the first POD coefficients means that higher order modes contribute to a certain extent to flow behavior, resulting in a higher amount of vortex cores and higher overall flow complexity. Figure 10b corresponds to image 484. In it, the first three POD coefficients were of a similar magnitude to the ones in Fig. 10a, but this time the third POD mode coefficient was positive. Figure 10b, however, does not present many vortex cores. Instead, two large symmetrical vortexes dominate the flow. An analysis of previous images shows that this is a snapshot of a mixed type vortex-shedding pattern, in which the alternating Karman vortexes are created from the merger of small vortexes.

Figure 11 shows eight consecutive snapshots of the flow immediately before the one presented in Fig. 10b. This is an upper view of the cylinder. The gray area represents the cylinder, and the black areas where the laser beam could not reach. It is possible to identify a Karman type of vortex shedding, but with some peculiarities. The four upper images describe the formation process of a clockwise rotating vortex. This vortex is clearly formed from the merging of many smaller vortexes. In the first image, there are three vortexes similar to those seen in Fig. 12a, which merge in the second frame. In the third fame, another vortex is formed at the upper side of the cylinder, while at the lower side there is already an anti-clockwise rotating vortex. In frame four, the new upper-side vortex is merging with the large clockwise vortex, whereas a series of complex vortex structures are formed at the lower side. Unfortunately, the vortexes at the bottom are not clear, but judging by the last four snapshots, the same process happens at the lower side.

The process described in Fig. 11 is a combination of anti-symmetrical and symmetrical vortex shedding patterns, with strong predominance of the former. This result indicates that a square cylinder's wake is governed by those two mechanisms, which interact in many ways to form mixed patterns, sometimes predominantly anti-symmetrical, sometimes symmetrical. Total data acquisition time was slightly more than one second, and a series of different flow conditions could be visualized, indicating either that small-scale variations in flow conditions can trigger strong variations in shedding patterns or that a lower frequency pattern governs which type of flow behavior predominates.
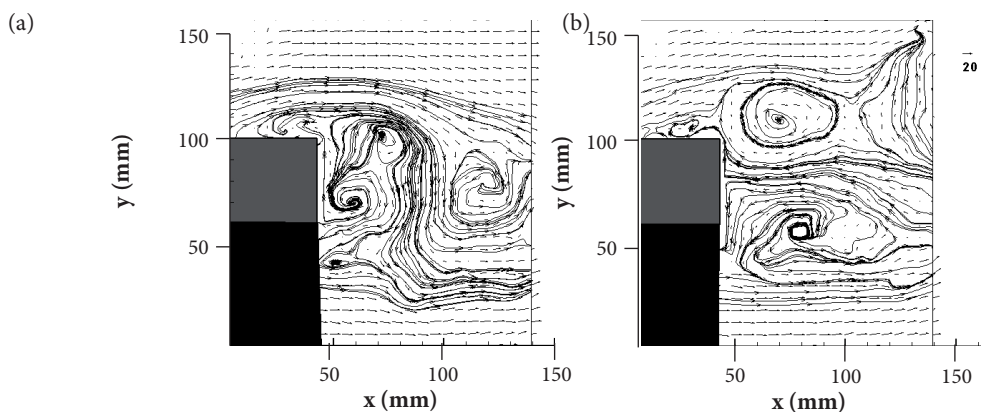
Figure 10. Instant velocity fields for an AR3 square section cylinder, z/h = 0.3. (a) Karman-like structure with multiple vortex cores; (b) strong symmetrical vortexes.
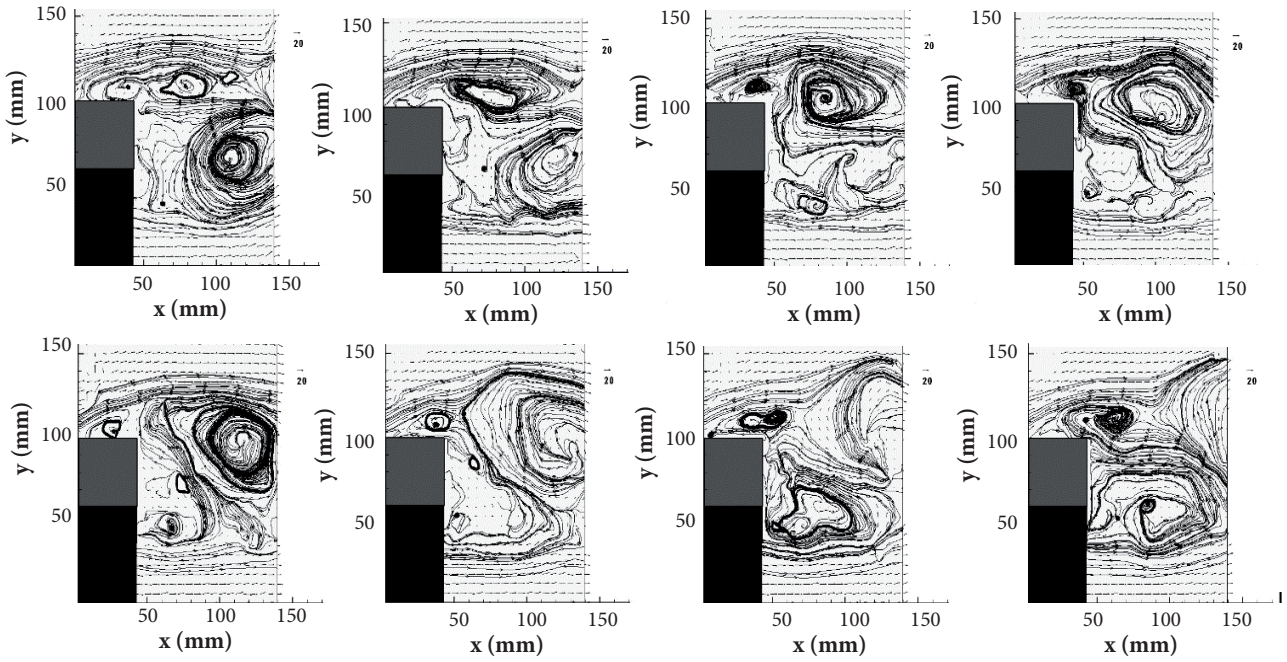
Figure 11. The vortex shedding pattern in a region of mixed POD mode predominance.
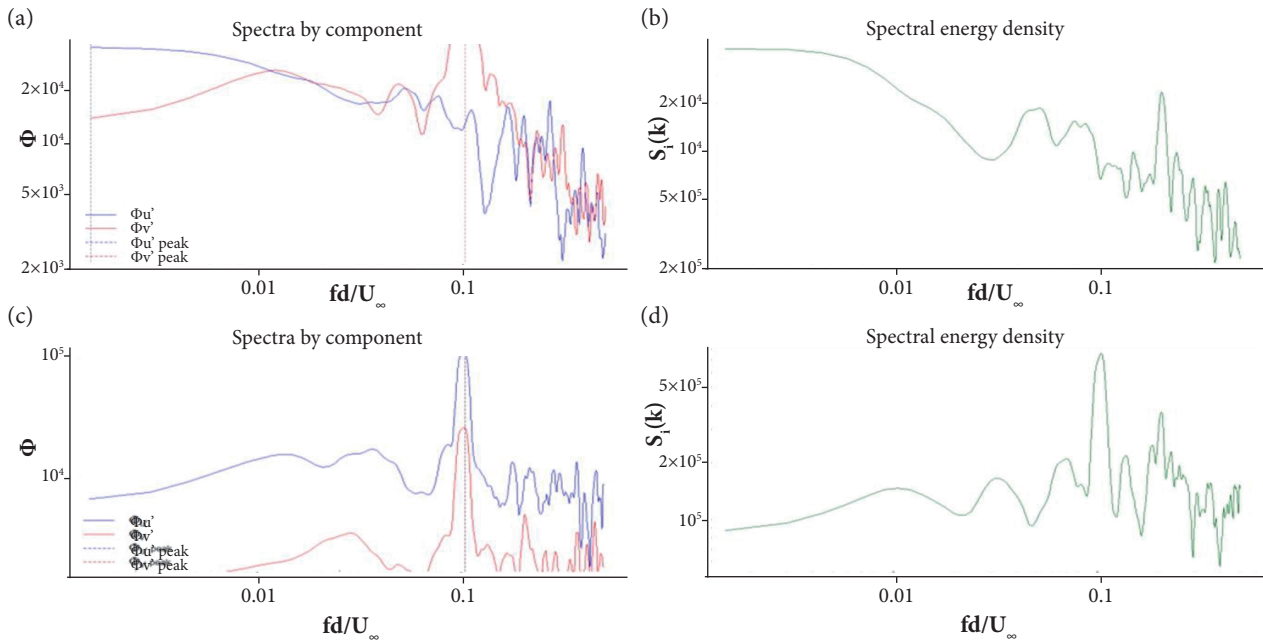
Figure 12. Spectral analysis for (a) *u* and *v* fluctuations; (b) TKE for a point at the core of POD mode 1 vortex; (c) *u* and *v* fluctuations and (d) TKE for a point at the core of POD mode 3 lateral elongated vortex.

To elucidate the questions that arise from our findings, larger data sets acquired during longer periods would be of great value. It is also important to understand the role of cylinder aspect ratio, mean flow velocity and cylinder geometry in this process, something the authors hope to explore in the near future.

SPECTRAL ANALYSIS

Spectral analysis was performed to a wide range of coordinates, but although there were some differences in the spectra, no discernible pattern was detected. Thus, only the results for two points are shown in Fig. 12. Figures 12a and 12b present the results for the analysis at the core of the vortex in POD mode 1, which can be seen in Fig. 4, whereas Figs. 12c and 12d represents results for the core of the lateral elongated vortex in POD mode 3. Even though the actual physical structures in the cylinder wake are moving, the selected points present minimum influence from modes 1 and 3, respectively, since at the vortex cores velocity is zero, and thus, their contribution to total velocity fluctuations at these points will be zero. Note that this process does not intend to isolate any particular flow structure, but the individual contribution of a particular POD mode.

With the exception of Fig. 12b, all spectra indicate a peak at $Sr = 0.103$, resulting in a vortex shedding frequency of 51.51 Hz. These results match both experimental data and numerical simulations very closely (Bourgeois *et al.* 2011; Wang *et al.* 2011), and are associated with the von Karman vortex shedding. For the POD mode 1 vortex core, only the *v* component presented a peak, while TKE analysis indicated a peak near $Sr = 0.2$, which is a harmonic of the shedding frequency. The absence of the $Sr = 0.1$ peak at the TKE and *u* velocity component spectrum indicates the effectiveness of the selected approach. By analyzing a point, were velocity fluctuations associated with POD mode 1 were zero, the frequency peak associated with this mode disappeared from the spectrum. There was still a peak for the *v* velocity component due to fluctuations associated with POD mode 2, which is also related to the von Karman vortex sheet, but which *u* component is almost zero at the chosen point. The results for the POD mode 3 vortex core show the same peak at $Sr = 0.103$, this time present in all three analyzed variables, as well as a secondary peak at $Sr = 0.2$ for the TKE.

From the comparison of these results, it is possible to conclude that the selected data point influences the analysis results considerably. The lack of a *u* component peak in Fig. 12a indicates that vortex induced *u* velocity component variations are of small relative importance when compared to fluctuations in other frequencies. This is probably an indication that this point is within the trajectory of the cores of most shed vortexes, which, supposing they are moving mostly streamwise, would induce strong *v* component variations, but weak *u* component ones. The result for TKE points to a relatively low importance of fluctuations in *v* for the turbulent kinetic energy, since its peak on $Sr = 0.103$ was not reflected on the TKE spectrum.

Results for the two other spectra, taken at the core of the symmetrical vortex in POD mode 3 do not indicate any frequency clearly associated with this mode. Frequency peaks near $Sr = 0.1$ were detected for all three parameters, again corroborating the hypothesis that *u* fluctuations play a greater role in TKE. A secondary peak near $Sr = 0.2$ was detected, corresponding to a harmonic. It is possible that the symmetrical vortex shedding frequency was masked by the much stronger anti-symmetrical one, making it undetectable at the first two spectra and therefore making the lack of its peak also undetectable at the POD mode 3 spectra. The use of filtering techniques capable of eliminating peaks correspondent to the anti-symmetrical shedding might help detecting other, less energetic peaks, if any.

CONCLUSION

The flow patterns over a square cylinder with aspect ratio $AR = 3$ were analyzed in a low horizontal plane, $z/h = 0.3$. Following a POD analysis, time-averaged and instant velocity fields were used to identify flow structures of interest. The POD modes 1 and 2, consistent with Karman vortex structures, contain more than half of the wake energy. Mode 2 shows a flow structure displaced about a quarter of the "vortex width" compared to mode 1. Modes 3 and 4, although representing only about 7% of the flow energy, were shown to play an important part in determining flow behavior. A scatter plot of the a_1 and a_2 coefficients shows a circular distribution, supporting the hypothesis that these modes represent a von Karman structure. Both symmetrical and anti-symmetrical shedding patterns were detected by POD analysis and instant velocity field visualizations. Instances of complex vortex shedding, with many small-scale vortexes were also identified, as well as predominantly anti-symmetrical but mixed type patterns, in which the influence of symmetrical modes caused the main vortexes to be formed by the merger of many small vortexes. All these structures could be detected by careful examination of the POD modes coefficients, proving the validity of this approach.

Spectral analysis indicated a peak at $Sr = 0.103$, corresponding to a frequency of 51 Hz. This result is associated with the von Karman vortex sheet and matched previous studies. The only other important peak was near $Sr = 0.2$, corresponding to a harmonic. Overall, spectral analysis was unable to indicate frequencies associated with less predominant vortex shedding modes, but by selecting specific points based on POD modes, selected frequency peaks could be suppressed. Therefore, although this technique failed to provide a symmetric mode shedding frequency, its validity was proven.

AUTHOR'S CONTRIBUTION

Experimental Data, Leite HF and Avelar AC; Conceptualization, Cavalieri A and Avelar AC; Investigation, Leite HF; Writing – Original Draft, Leite HF, Abreu L and Schuch D; POD computational code, Abreu L and Cavalieri A; Spectral Analysis, Schuch D; Writing – Review and Editing, Avelar AC and Cavalieri A.

REFERENCES

Adaramola MS, Akinlade OG, Sumner D, Bergstrom DJ, Schenstead AJ (2006) Turbulent wake of a finite circular cylinder of small aspect ratio. J Fluids Struct 22:919-928. doi: 10.1016/j.jfluidstructs.2006.04.007

Bourgeois JA, Sattari P, Matinuzzi RJ (2011) Alternating half-loop shedding in the turbulent wakeof a finite surface-mounted square cylinder with a thin boundary layer. Phys Fluids 23, Paper no. 095101-1. doi: 10.1063/1.3623463

Etzold F, Fiedler H (1976) The near-wake structure of a cantilevered cylinder in a crossflow. Z Flugwiss 24:77-82.

Graftieaux L, Michard M, Grosjean N (2001) Combining PIV, POD and vortex identification algorithms for the study of unsteady turbulent swirling flows. Meas Sci Technol 12:1422-1429. doi: 10.1088/0957-0233/12/9/307

Holmes P, Lumley JL, Berkooz G (1998) Turbulence, coherent structures, dynamical systems and symmetry. Cambridge, United Kingdom: Cambridge University Press.

Hosseni Z, Bourgeois JA, Martinuzzi RJ (2012) Wall-mounted finite cylinder wake structure modification due to boundary layer-wake interaction: Half-loop and full-loop coherent structure topologies. Proceedings of the 7th International Colloquium on Bluff Body Aerodynamics and Applications (BBAA7), V. 1, International Association for Wind Engineering; Shanghai.

Kaimal JC, Finnigan JJ (1994) Atmospheric boundary layer flows. Their structure and measurement. Cambridge, United Kingdom: Oxford University Press. p. 289.

Kawamura T, Hiwada M, Hibino T, Mabuchi I, Kumada M (1984) Flow around a finite circular cylinder on a flat plate. Bulletin of JSME 27(232):2142-2151.

Levold P (2012) Viscous flow around finite length circular cylinder (Master of Science degree thesis). Trondhein, Norway: Norwegian University of Science and Technology.

Leite HF, Avelar AC, De Abreu LI, Schuch D (2016) POD and spectral analysis of a wall-mounted square cylinder wake. Proceedings of EPTT, V. 1, ABCM; Rio de Janeiro.

Meyer KE, Pedersen JM, Ozcan O (2007) Turbulent jet in crossflow analyzed with proper orthogonal decomposition. J Fluid Mech 583:199-227. doi: 10.1017/s0022112007006143

Okamoto T, Yagita M (1973) The experimental investigation on the flow past a circular cylinder of finite length placed normal to the plane surface in a uniform stream. Bull JSME 16:805-814. doi: 10.1299/jsme1958.16.805

Park CW, Lee SJ (2002) Flow structure around a finite circular cylinder embedded in various atmospheric boundary layers. Fluid Dyn Res 30:197-215. doi: 10.1016/s0169-5983(02)00037-0

Pattenden RJ, Turnok SR, Zhang X (2005) Measurements of the flow over a low aspect ratio cylinder mounted on a ground plane. Exp Fluids 39(1):10-21. doi: 10.1007/s00348-005-0949-9

Pedersen JM, Meyer KE (2002) POD analysis of flow structures in a scale model of a ventilated room. Exp Fluids 33(6):940-949. doi: 10.1007/s00348-002-0514-8

Roh SC, Park S (2003) Vortical flow over the free end surface of a finite circular cylinder mounted on a flat plate. Exp Fluids 34:63-67. doi: 10.1007/s00348-002-0532-6

Sakamoto H, Arie M (1983) Vortex shedding from a rectangular prism and a circular cylinder placed vertically in a turbulent boundary layer. J Fluid Mech 126:147-165. doi: 10.1017/S0022112083000087

Sakamoto H, Oiwake S (1984) Fluctuating forces on a rectangular prism and a circular cylinder placed vertically in a turbulent boundary layer. J Fluids Eng 106:160-166. doi: 10.1115/1.3243093

Tanaka S, Murata S (1999) An investigation of the wake structure and aerodynamic characteristics of a finite circular cylinder. JSME Int J Ser B Fluids Therm Eng 42:178-187. doi: 10.1299/jsmeb.42.178

Uematsu Y, Yamada M, Ishii K (1990) Some effects of free-stream turbulence on the flow past a cantilevered circular cylinder. J Wind Eng Ind Aerodyn 33:43-52. doi: 10.5359/jawe.1988.37_83

Wang G (2015) PIV experiment and CFD simulation of flow around cylinder (Master of Science degree thesis). Austin, Texas, USA: University of Texas.

Wang H (2012) POD analysis of the finite-length square cylinder wake. Proceedings of the 7th International Colloquium on Bluff Body Aerodynamics and Applications (BBAA7); Shanghai, China.

Wang HF, Zhou Y (2009) The finite-length square cylinder near wake. J Fluid Mech 638:453-491. doi: 10.1017/s0022112009990693

Wang HF, Zhou Y, Chan CK (2005) Flow around a finite length square prism. Proceedings of the 4th European and African Conference on Wind Engineering Institute of Theoretical and Applied Mechanics, Academy of Sciences of the Czech Republic; Prague.

Wang HF, Zhou Y, Chan CK, Lam KS (2006) Effect of initial conditions on interaction between a boundary layer and a wall-mounted finite-length-cylinder wake. Phys Fluids 18(6):065106. doi: 10.1063/1.2212329

Wang YQ, Jackson P, Sui J (2011) Simulation of flow around a surface-mounted square-section cylinder of aspect ratio four. Proceedings of the 20th Annual Conference of the CFD Society of Canada; Canmore, AB, Canada.

Williamson CHK (1996) Vortex dynamics in the cylinder wake. Annu Rev Fluid Mech 28:477-539. doi: 10.1146/annurev.fluid.28.1.477